Clays and Clay Minerals (2024), **72**, e1, 1–12
doi:10.1017/cmn.2024.1

Original Paper

Variation in the structural order of kaolinite in regolith as an effective indicator of REE mineralization

Lianying Luo[1,2,3], Wei Tan[1,2], Xiaorong Qin[1,2,3], Shichao Ji[1,2], Xiaoliang Liang[1,2,3] and Hongping He[1,2,3]

[1]CAS Key Laboratory of Mineralogy and Metallogeny/Guangdong Provincial Key Laboratory of Mineral Physics and Materials, Guangzhou Institute of Geochemistry, Chinese Academy of Sciences, Guangzhou, China; [2]CAS Center for Excellence in Deep Earth Science, Guangzhou, China and [3]University of Chinese Academy of Sciences, Beijing, China

Abstract

Regolith-hosted rare earth element (REE) deposits hosted by the granitic regolith in South China provide >90% of the world's heavy REEs. Kaolinite is one of the major carriers of REE ions in regolith. The formation and transformation of kaolinite can be affected by chemical weathering and hydrodynamic conditions, but the contribution of each factor has not been evaluated. This study systematically investigated the variation in abundance of phyllosilicate minerals and structural order of kaolinite in the Renju regolith-hosted REE deposit. The total abundance of 1:1 phyllosilicate minerals increased upwards along the profile from Section I to Section III. However, semi-quantitative analyses indicated that Section III-1 (depth at 10–16 m) featured an evident decrease in both abundance and structural order of kaolinite upward along the profile. The morphological feature and abundance of kaolinite revealed intensive kaolinite-to-halloysite transformation and kaolinite dissolution in Section III-1. This suggests that the alternating wetting and drying zone in Section III-1 provided a favorable kinetic environment for the entry of water molecules into the kaolinite interlayer and the kaolinite-to-halloysite transformation, resulting in both lower structural order and abundance of kaolinite in Section III-1. Moreover, REE ions started to be enriched from the alternating wetting and drying zone and formed high-grade ores at the lower part of the water table, due to a significant increase in pore water and decrease in the seepage velocity. Therefore, the abundance and structural order of secondary kaolinite can serve as important indicators of hydrodynamic changes in regolith, as well as the mineralization of regolith-hosted REEs.

Keywords: halloysite; kaolinite; regolith-hosted REE deposit; structural order; X-ray diffraction

(Received: 27 October 2023; revised: 12 January 2024; accepted: 12 February 2024)

Introduction

Regolith-hosted rare earth element (REE) deposits in South China provide >90% of the world's heavy REEs, which are critical to modern society and high-end technology (Bao and Zhao, 2008; Simandl, 2014; Weng *et al.*, 2015; Jowitt *et al.*, 2017; Riesgo García *et al.*, 2017; Xu *et al.*, 2017). These deposits are hosted by regolith developed from biotite and muscovite granites, syenites, monzogranites, granodiorites, granite porphyries, and rhyolitic tuffs (Li *et al.*, 2017). During the formation of regolith, humic acid, organic acid and CO_2, which are produced by decay of organic matter and the activity of microorganisms and vegetation (McQueen and Scott, 2008), acidify surface and groundwater. REE-bearing minerals (*e.g.* synchysite and titanite) tend to be dissolved by the acidified water, and the released REE are leached downward vertically in the regolith and adsorbed onto the surface of secondary phyllosilicate minerals weathered from primary rock-forming minerals, forming regolith-hosted REE deposits (Bao and Zhao, 2008; Huang *et al.*, 2021a).

During weathering, primary minerals (such as feldspar and mica) are first altered into the incipient 2:1 phyllosilicate minerals (*e.g.* illite and smectite), before further transforming into the 1:1 phyllosilicate minerals (*e.g.* halloysite and kaolinite) (Senkayi *et al.*, 1984; Li and Zhou, 2020). Consequently, illite and smectite are predominant in the saprock and saprolite, while the abundance of kaolinite and halloysite increases in the more weathered shallow zones of the regolith (Mei *et al.*, 2021; Tan *et al.*, 2021). Compared with the lower pedolith zone, vermiculite and well-ordered kaolinite appear in the upper pedolith zone, whereas the abundance of halloysite decreases (Li and Zhou, 2023). Accordingly, the vertical zonation in well-developed profiles of regolith can be defined by the mineral abundance and structural order of kaolinite and other phyllosilicates (Huang *et al.*, 2021a; Tan *et al.*, 2021).

Kaolinite has been suggested as the primary carrier of REE ions in regolith (Yang *et al.*, 2019; Borst *et al.*, 2020). Notably, REEs tend to be enriched in the vicinity of the transition zone between upper and lower pedolith (Li and Zhou, 2023), possibly due to the different REE adsorption capacity of the clay minerals caused by significant changes in the structural order of kaolinite during chemical weathering (Fialips *et al.*, 2000; Ndlovu *et al.*, 2015; Li and Zhou, 2020, 2023). However, the changes in the crystallographic and physicochemical properties of kaolinite may also be affected by

Corresponding author: Wei Tan; Email: tanwei@gig.ac.cn
Cite this article: Luo L., Tan W., Qin X., Ji S., Liang X., & He H. (2024). Variation in the structural order of kaolinite in regolith as an effective indicator of REE mineralization. *Clays and Clay Minerals* **72**, e1, 1–12. https://doi.org/10.1017/cmn.2024.1

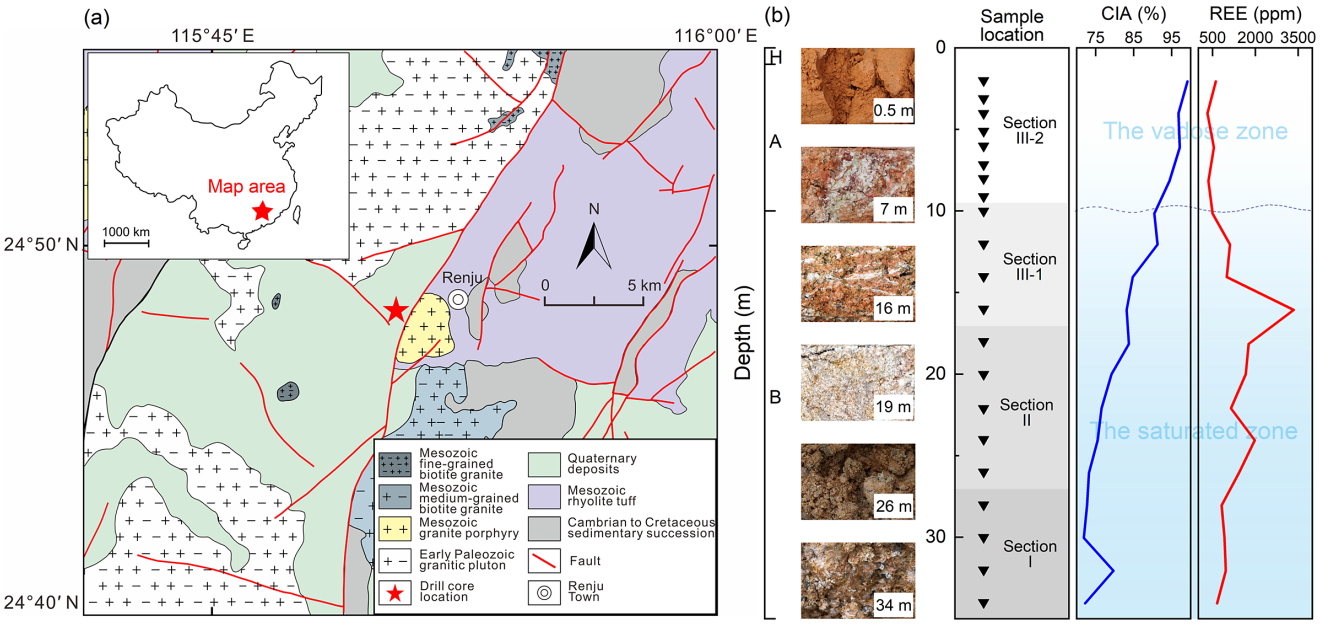

Figure 1. (a) Simplified geologic map of the Renju regolith-hosted REE deposit, revised according to the report of the Regional Geological Survey Team of Jiangxi Geological Bureau (1976). (b) Original data sets of REE concentrations, the chemical index of alteration (CIA) values, and depth of the vadose zone–saturated zone boundary were obtained from Huang *et al.* (2021a).

the hydrodynamic conditions. For example, dry conditions above the water table have been suggested as favorable for kaolinite crystallization (Costanzo and Giese, 1985; Inoue *et al.*, 2012). The overlapping roles of chemical weathering and hydrodynamic effects on the formation and transformation of kaolinite, especially for the structural order of kaolinite, have not been explicated. Additionally, the downward migration and enrichment behaviors of REEs could also be controlled by the notable variations in hydrodynamic properties of regolith due to presence of the water table (Huang *et al.*, 2021a). The underlying relationship between REE mineralization and the transformation behaviors of kaolinite in regolith also requires further elucidation.

This study established systematic variations in abundance of different types of phyllosilicate minerals and structural order of kaolinite in the Renju regolith-hosted REE deposits in South China. The mutual transformation between kaolinite and halloysite was also revealed via scanning electron microscopy (SEM) and transmission electron microscopy (TEM). The obtained data sets were used to explore the factors governing the phyllosilicate mineral in the formation of regolith-hosted REE deposits. This study highlights the influence of hydrodynamic conditions on the transformation behaviors of kaolinite and the genesis of regolith-hosted REE deposits.

Renju regolith-hosted REE deposit

The Renju REE deposit is located in northeast Guangdong, South China. The total rare earth oxide (REO) resources of the Renju deposit have been estimated as ~20,000 tons, with an average grade of ore body ranging from 0.153 to 0.197 wt.% (Wang and Xu, 2016). More than 70% of the REEs in the deposit occur as exchangeable ions (Yang and Xiao, 2011). The deposits were developed in hills, with elevations varying from 250 to 350 m above sea-level and slope gradients generally <25° (Huang *et al.*, 2021a). The Renju area is characterized by the subtropical monsoon climate, with an average temperature of 20.6°C, and annual precipitation of 1500–2000 mm (Huang *et al.*, 2021b), which is favorable for the chemical weathering of granitoid rocks and the further formation of thick regolith. This monsoon climate formed before 41 Ma and became modern-like after 26 Ma, as recorded by stratigraphy and paleoclimate proxies, *e.g.* pollen content of xerophytic plants (Wu *et al.*, 2022).

The regolith hosting the REE deposit developed on bedrock of Mesozoic quartz diorite, granite porphyry, and biotite granite (Huang *et al.*, 2021b; Zhao *et al.*, 2021). Ore bodies containing >500 ppm REEs occur in the completely weathered zone (depths of 10–34 m) of the regolith (Fig. 1; Table 1). Based on the systematic variations in Fe oxide and Ce anomaly, the boundary between the vadose and saturated zones in the Renju regolith was estimated at a depth of 10 m (Huang *et al.*, 2021a).

Sampling and methods

Sampling

Samples were selected from a 34 m drill core in the Renju REE deposit. The exposed topsoil (~1 m) was removed, and a total of 21 bulk samples were selected from depths ranging from ~2 to 34 m, with intervals of 1–2 m. The whole-rock samples were dried at room temperature and milled into 200 mesh powders. The clay fractions (equivalent spherical diameter <2 μm) (Schroeder, 2018) were concentrated by dispersing the whole-rock samples using a sodium hexametaphosphate solution in an ultrasonic bath and extracting the uppermost sedimentation according to the principles of Stokes' law. The clay fractions were subsequently freeze-dried. The whole-rock samples were used for identification and semi-quantification of primary and secondary minerals. The clay fractions were used for phase identification, semi-quantitative analysis of the various phyllosilicate mineral phases, and evaluation of the structural order of kaolinite.

https://doi.org/10.1017/cmn.2024.1 Published online by Cambridge University Press

Table 1. Summary of the geochemical and mineralogical characteristics of the Renju regolith-hosted REE deposit

			Abundance (wt.%)				Structural order				
Depth (m)	Section	CIA (%)	Clay	Kln	Hly	Ilt	HI	R2	Whole-rock REE (ppm)	iREE (ppm)	REE adsorption capacity (ppm)
2	Section III–2	99	84	77	6	1	0.66	1.02	607	159	2661
3			73	66	5	2	0.73	1.03			2302
4		97	69	54	12	3	0.68	0.97	315		2050
5			70	58	10	2	0.58	0.98			2146
6		97	77	56	18	3	0.63	0.86	537	148	2225
7			77	36	39	2	0.32	0.85			1870
8		94	74	51	21	2	0.53	0.87	354		2105
9			68	48	19	1	0.27	0.85			1971
10	Section III–1	90	71	22	48	1	0.42	0.84	501	366	1542
12		91	75	14	55	6	0.45	0.79	1107	659	1366
14		85	61	40	15	5	0.49	0.90	996		1646
16		83	73	58	11	4	0.65	0.95	3343	2163	2177
18	Section II	84	60	27	31	2	0.45	0.87	1761		1453
20		79	61	34	25	2	0.51	0.95	1661	1222	1569
22		77	59	45	9	6	0.76	1.05	1143		1692
24		76	57	23	27	7	0.53	0.98	1976	1220	1215
26		73	59	37	7	14	0.77	0.98	1420		1405
28	Section I	73	53	33	16	3	0.48	0.99	817	669	1421
30		72	43	39	2	2	0.78	0.99	918		1367
32		80	47	40	4	3	0.53	0.94	966	640	1453
34		72	54	46	4	4	0.65	1.00	660		1647

The original data for chemical index of alteration (CIA), whole-rock rare earth element (REE), and ion-exchangeable REE (iREE) are from Huang *et al.* (2021a).

Methods

X-ray diffraction (XRD)

The analyses were performed using a Rigaku MiniFlex-600 X-ray diffractometer in the Key Laboratory of Mineralogy and Metallogeny, Guangzhou Institute of Geochemistry, Chinese Academy of Sciences. The diffraction patterns were recorded by a 1 D detector, using CuKα radiation filtered with Ni operated at a current of 15 mA and voltage of 40 kV. The mineral phases were analyzed using JADE 6.5, referring to standard PDF cards from the International Centre for Diffraction Data (ICDD®) (Blanton and Gates-Rector, 2019).

Phase identification. Randomly oriented powders of the whole-rock samples were scanned from 3 to 80°2 at 10°2θ min^{-1}. The diffractions at ~3.3 and 4.3 Å were related to quartz, and the diffraction at ~3.3 Å was derived from orthoclase. The basally oriented powders of the clay fraction samples were prepared by pipetting the water-dispersed samples onto glass slides and air-drying. The basally oriented powders were then scanned at 3°2θ min^{-1} from 3 to 30°2θ. The diffraction at 10 Å was related to illite and halloysite, and the diffraction at 7.2 Å was related to kaolinite and halloysite. The 120°C-heated samples were prepared by heating the basally oriented samples in an oven at 120°C for 6 h, so that the interlayer water in halloysite-10 Å was lost due to heating (Joussein *et al.*, 2006). The diffraction at 10 Å was mostly derived from illite in the 120°C-heated samples. The formamide-intercalated samples were prepared by intercalating the 120°C-heated samples with formamide for 20 min (Churchman *et al.*, 1984). The diffraction at 7.2 Å was mostly derived from kaolinite in the formamide-intercalated samples, as the halloysite-7 Å had expanded to 10 Å due to intercalation. The 120°C-heated and formamide-intercalated samples were scanned at 3°2θ min^{-1} from 3 to 30°2θ.

Semi-quantification of mineral abundance. Semi-quantitative analyses were performed using a ratio method (Chung, 1974) based on the diffraction area of each mineral using:

$$W_\rho = \frac{\frac{S_\rho}{K^\rho_{cor}}}{\sum_{j=1}^{n} \frac{S_j}{K^j_{cor}}}, \quad (1)$$

where W_ρ refers to the abundance of mineral ρ; S_ρ refers to the area of the most intense diffraction of mineral ρ; and K^ρ_{cor} refers to the reference intensity ratio (RIR) value of mineral ρ.

Structural order of kaolinite. The clay fractions were used for characterizing the structural order of kaolinite. Randomly oriented powders of clay fractions were scanned from 3 to 70°2θ at 3° 2θ min^{-1} for evaluation the structural order of kaolinite, based on the XRD pattern in the ranges of 20–23°2θ and 35–40°2θ (Fialips *et al.*, 2000; Bauluz *et al.*, 2008; Ni *et al.*, 2021). Effective XRD indices include the Hinckley index (HI), Liétard index (R2), Stoch index (IK), Range and Weiss index (QF), and full width at half maximum

https://doi.org/10.1017/cmn.2024.1 Published online by Cambridge University Press

(Aparicio and Galan, 1999; Zadvernyuk *et al.*, 2021). Among them, HI and R2 are commonly used to characterize the defect structures of kaolinites (Fialips *et al.*, 2000; He *et al.*, 2005; Ishida *et al.*, 2018; Pineau *et al.*, 2022). The kaolinite structural order indices used for this study were HI Eqn 2; Hinckley, 1962) and R2 Eqn 3; Liétard, 1977) according to the powder XRD patterns using:

$$\mathrm{HI} = \frac{A+B}{At}, \tag{2}$$

and

$$\mathrm{R2} = \frac{\frac{1}{2}(K1+K2)-k}{\frac{1}{3}(K1+K2+k)}, \tag{3}$$

where A is the height of the $(1\bar{1}0)$ diffraction peak to the background line drawn from the trough between (020) and $(1\bar{1}1)$; B is the height of the $(1\bar{1}1)$ diffraction peak to the background line drawn from the trough between (020) and $(1\bar{1}1)$; At is the height of the $(1\bar{1}0)$ diffraction peak above the general background; $K1$ is the height of the (131) diffraction peak; $K2$ is the height of the $(1\bar{3}1)$ diffraction peak; and k is the height of the trough between $(1\bar{3}1)$ and (131).

Accordingly, kaolinite of different structural orders can be classified into low-defect kaolinite (HI=0.90−1.15; R2>1.20), medium-defect kaolinite (HI=0.50–0.90; R2=0.70–1.20), and high-defect kaolinite (HI<0.50; R2<0.70) (Aparicio *et al.*, 2006).

REE adsorption capacity calculation

The REE adsorption capacity (AC) of regolith was calculated by summing the REE adsorption capacity of each phyllosilicate mineral in a regolith using:

$$\mathrm{AC} = \sum_{\rho=1}^{n} W_\rho C_\rho, \tag{4}$$

where W_ρ refers to the abundance of mineral ρ; and C_ρ refers to the saturated REE adsorption capacity of mineral ρ. The REE AC was calculated mainly based on the AC of kaolinite and halloysite, which accounts for 85–100% of the total abundance of phyllosilicate minerals in the regolith. The kaolinite and halloysite REE AC values used for calculation were 3460 and 1610 ppm (at pH=5), which were experimentally determined by Yang *et al.* (2019).

The concentration of whole-rock REE (Table 1) was obtained by analyzing the whole-rock powders (200 mesh) using a Thermo iCAP Qc inductively coupled plasma-mass spectrometer (ICP-MS) (Huang *et al.*, 2021a). Before the ICP-MS analysis, the samples were dried at 105°C for 3 h and then baked at 550°C for 3 h to eliminate organic material. Approximately 0.04 g of each solid sample was analyzed. Rh was added to each sample as an internal standard to calibrate the drift of the instrument during the measurements. The analytical precision for the whole-rock REE content was better than 3% RSD (Relative Standard Deviation).

The concentration of ion-exchangeable REE (iREE) (Table 1) represents the REE ions adsorbed by clay minerals in the regolith. The concentration of iREE was acquired by mixing 1.00 g of powdered whole-rock samples (200 mesh) with 25 mL of 1.0 mol L^{-1} MgCl solution (pH=7±0.2) in centrifuge tubes. The centrifuge tubes were then shaken at room temperature (25±0.2°C) for 2 h, after which the supernatant was collected for ICP-MS analysis (Huang *et al.*, 2021a).

Scanning electron microscopy

The bulk samples were embedded with epoxy and subsequently made into thin-section samples. The thin sections were coated with carbon for SEM analyses. The paragenesis characteristics of phyllosilicate minerals in the Renju REE deposit were investigated using a MIRA3 TESCAN scanning electron microscope in the secondary electron mode at a voltage of 20 kV. The surface elemental composition was characterized using an EDAX Element EDS detector for phyllosilicate identification.

Transmission electron microscopy

The separated clay fractions were ultrasonically dispersed in ethanol, and the suspension was transferred onto a porous carbon film supported by a copper grid. Nano-scale morphological features of the phyllosilicate minerals were examined using a transmission electron microscope (Thermo Scientific FEI Talos F200S) at 200 kV.

Results

Phyllosilicate minerals in the Renju regolith

Composition of phyllosilicate minerals

All XRD patterns for randomly oriented whole-rock samples showed sharp XRD peaks of quartz at ~3.3 and 4.3 Å (Fig. 2).

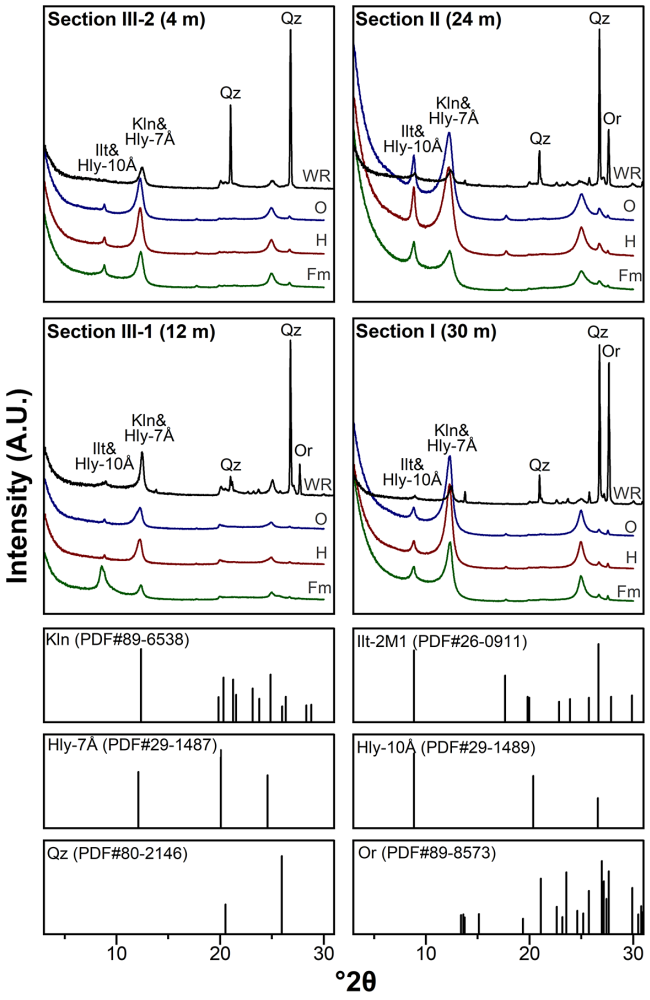

Figure 2. X-ray diffraction (XRD) patterns of randomly oriented whole-rock samples and oriented clay fractions (<2 μm) from various sections. WR = whole-rock powder XRD samples; O = basally oriented samples; H = 120°C-heated samples; Fm = formamide-intercalated samples; Kln = kaolinite; Hly = halloysite; Ilt = illite; Qz = quartz; Or = orthoclase.

https://doi.org/10.1017/cmn.2024.1 Published online by Cambridge University Press

The diffraction of orthoclase at ~3.3 Å presented in samples from the depth of 10–34 m in the regolith, but disappeared in the samples <10 m from the top (Fig. 2). The profiles featured characteristic diffractions at ~7.2 and 10 Å. The 10 Å diffraction corresponded to a mixture of the (001) plane of illite and the (001) plane of halloysite-10 Å, and the 7.2 Å diffraction corresponded to the (001) plane of kaolinite and the (001) plane of halloysite-7 Å. Specifically, for the heated samples, the decrease in diffraction intensities at 10 Å (I_{10}) was consistent with the increase in diffraction intensities at 7.2 Å ($I_{7.2}$), and the $I_{7.2}/I_{10}$ ratios of the heated samples were 3–15% higher than those of the basally oriented samples, suggesting the presence of halloysites at ~10 Å. Moreover, the formamide-intercalated samples exhibited a decrease in the diffraction intensities at ~7.2 Å and an equivalent increase at ~10 Å compared with the basally oriented samples (Fig. 2). Accordingly, the 28–72% decrease in the $I_{7.2}/I_{10}$ ratios was attributable to the expansion of halloysite (001) plane from ~7.2 to 10 Å (Churchman and Theng, 1984; Churchman and Gilkes, 1989). The diffraction at ~7.2 Å of the formamide-intercalated samples and diffractions at ~10 Å of the heated samples in the profiles were contributed by kaolinite and illite, respectively.

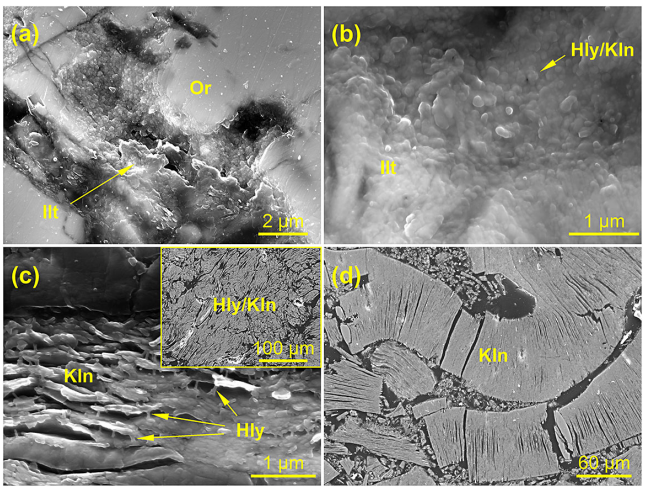

Figure 4. Secondary electron micrograph of minerals in (a) Section I, (b) Section II, (c) Section III-1, and (d) Section III-2. The upper right inset in (c) presents the phyllosilicate mineral aggregations in Section III-1. Kln = kaolinite; Hly = halloysite; Ilt = illite; Or = orthoclase.

Abundance of phyllosilicate minerals

The abundance of total phyllosilicate minerals fluctuated between 40 and 85 wt.% (Fig. 3; Table 1). Kaolinite and halloysite were the dominant secondary phyllosilicate minerals, accounting for 40–80 wt.% of the regolith sample. According to the abundance and distribution of the phyllosilicate minerals, the investigated regolith can be divided into three sections, and Section III can be subdivided into two sections; these sections were numbered from the completely weathered zone upward to the topsoil.

Section I was located at a depth ranging from 28 to 34 m, and was characterized by a relatively small abundance (43–54 wt.%) of phyllosilicate mineral. Phyllosilicate minerals commonly occurred along the micro-fractures and grain boundaries of the weathered primary minerals as aggregations of <10 μm (Fig. 4a). The abundance of kaolinite decreased from 46 to 33 wt.% upward along the profile, whereas the abundance of halloysite increased from 4 to 16 wt.%, and that of illite fluctuated between 2 and 4 wt.% (Fig. 3; Table 1).

Section II was located at a depth ranging from 18 to 28 m and was characterized by a relatively large abundance (57–61 wt.%) of phyllosilicate minerals. In this section, the abundance of kaolinite fluctuated between 23 and 45 wt.%. Notably, the abundance of halloysite continually increased from 7 to 31 wt.% upward along the profile in Section II, whereas the abundance of illite decreased significantly from 14 to 2 wt.% (Fig. 3; Table 1). The size of phyllosilicate minerals examined by SEM exceeded 20 μm. The phyllosilicate minerals were identified based on the EDS results

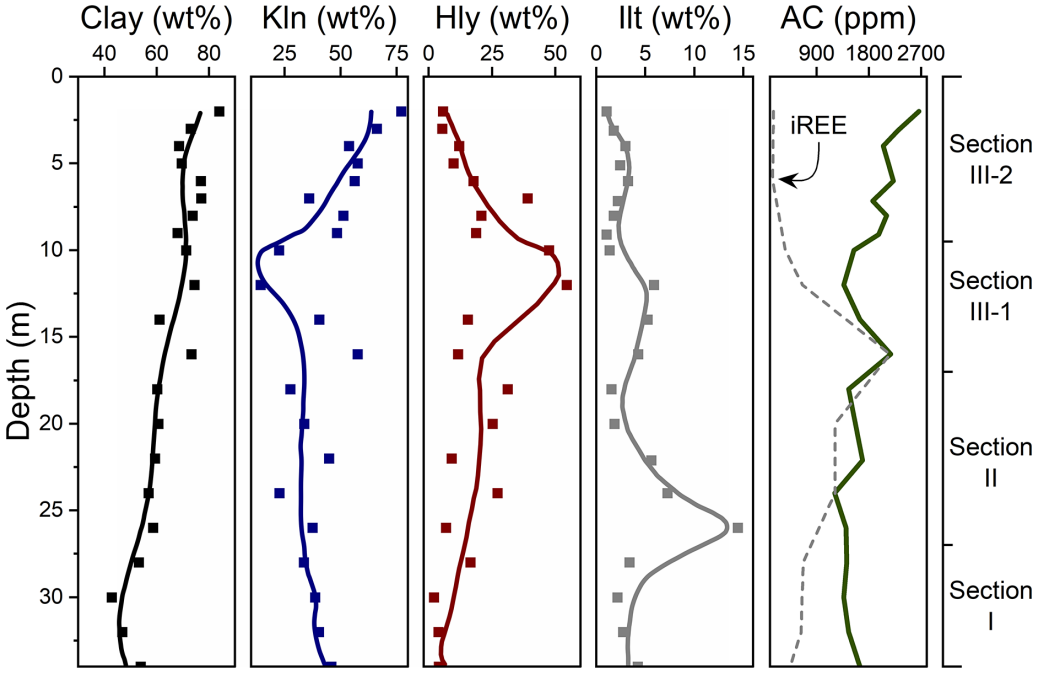

Figure 3. Variation in the abundances of phyllosilicate minerals (clay), kaolinite (Kln), halloysite (Hly), illite (Ilt), ion-exchangeable REE (iREE), and REE adsorption capacity (AC) along the profile of the Renju regolith-hosted REE deposit. The iREE data were obtained from Huang *et al.* (2021a).

https://doi.org/10.1017/cmn.2024.1 Published online by Cambridge University Press

(Fig. S1). The 2:1 phyllosilicate mineral (illite) showed Si to Al ratios close to 2:1, and the 1:1 phyllosilicate mineral (kaolinite and halloysite) approaching 1:1. The 1:1 type kaolinite and halloysite microcrystals occurred at the edge of 2:1 type illite grains (Fig. 4b).

Section III was located at a depth ranging from 2 to 18 m, and the total phyllosilicate mineral abundance was 60–85 wt.%. The section was dominated by 1:1 phyllosilicate minerals, and the phyllosilicate mineral aggregations usually exceeded 100 μm. According to the distinctive variations in the abundances of kaolinite and halloysite, Section III can be subdivided into Sections III-1 and III-2.

Section III-1 was located at a depth ranging from 10 to 18 m. The abundance of halloysite in this section increased significantly from 12 to 55 wt.% upward along the profile, whereas the abundance of kaolinite decreased sharply from 58 to 14 wt.%. The abundance of illite ranged between 1 and 6 wt.% (Fig. 3; Table 1). The phyllosilicate minerals form irregular aggregates with massive 100–500 nm interstices, and the interstices between kaolinite plates were filled with curved halloysite tubes (Fig. 4c).

Section III-2 was located at a depth ranging from 2 to 10 m in the regolith. The abundance of kaolinite increased abruptly from 48 to 74 wt.% upward along the profile, while the abundance of halloysite decreased significantly from 19 to 6 wt.%. The abundance of illite decreased from 3 to 1 wt.% (Fig. 3; Table 1). The kaolinite plates featured regular pseudo-hexagonal edges and formed aggregates occurring as vermicular booklets (Fig. 4d).

Structural order of kaolinite

The HI and R2 values are shown in Fig. 5 and Table 1. For Section I, the HI and R2 values fluctuated along the section between 0.48 to 0.78 and 0.94 to 1.00, respectively. The corresponding TEM results revealed that kaolinite aggregates in this section were mainly composed of thinner plates in face–face contact and featured a relatively pseudo-hexagonal morphology (Fig. 6a,b).

For Section II, the HI and R2 values slightly decreased upward along the profile, with HI varying from 0.77 to 0.45 and R2 varying from 0.98 to 0.87. The morphologies of kaolinite aggregates showed little change along the profile, and kaolinite plates with flat edges were stacked to form pseudo-hexagonal kaolinite aggregates (Fig. 6c,d).

For Section III-1, the HI and R2 values decreased abruptly from 0.65 to 0.42 and 0.95 to 0.84 upward along the profile, respectively. Some kaolinite aggregates exhibited complex surface morphologies, featuring rounded edges and uneven surfaces, and the aggregates contained fewer kaolinite plates. In addition, some kaolinite plates with relatively flat edges curled at the edges at different angles and formed halloysite tubes and spheres (Fig. 6e,f).

For Section III-2, the HI value increased from 0.27 at the bottom to 0.67 at the top. Similarly, R2 increased from 0.85 at the bottom to 1.02 at the top. Kaolinite plates with relatively straight boundaries and angular edges aggregated and formed regularly shaped aggregates, and the tubular halloysite began to unfold (Fig. 6g,h).

REE adsorption capacity

The simulative REE adsorption capacity results are shown in Table 1 and Fig. 3. REE adsorption capacity in Section I and Section II fluctuated between 1215 and 1692 ppm, then decreased from 2177 to 1542 ppm from the bottom to the top of Section III-1, and finally increased from 1971 to 2661 ppm from the bottom to the top of Section III-2.

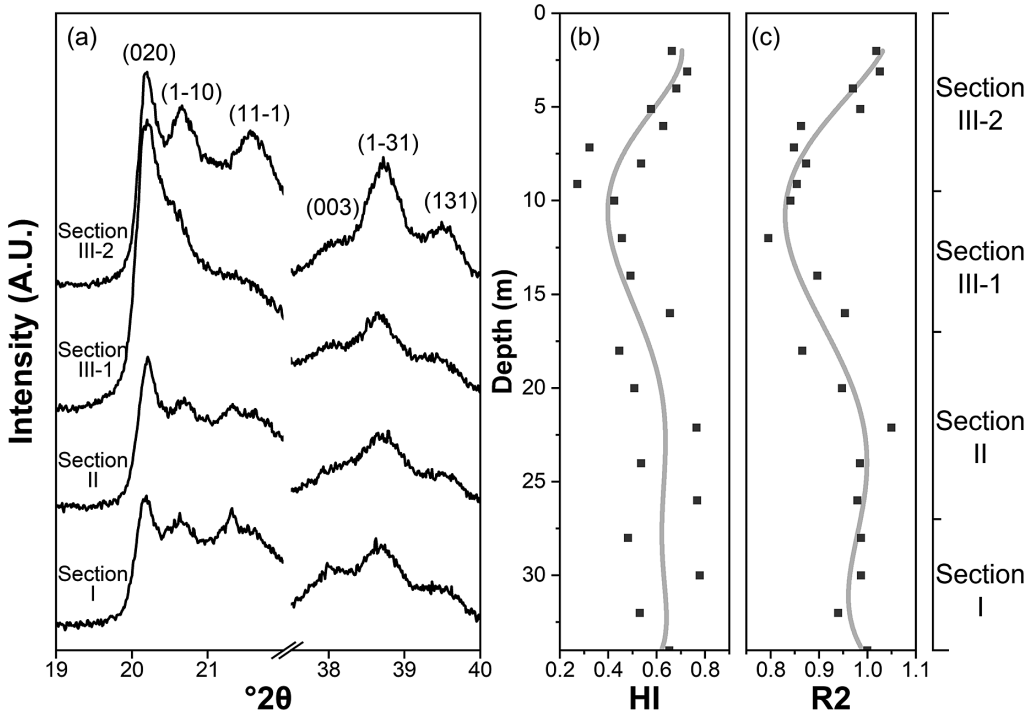

Figure 5. (a) X-ray diffraction patterns of randomly oriented clay fractions (<2 μm) from various depths, and variation in (b) the Hinckley index (HI) and (c) the Liétard index (R2) along the profile.

https://doi.org/10.1017/cmn.2024.1 Published online by Cambridge University Press

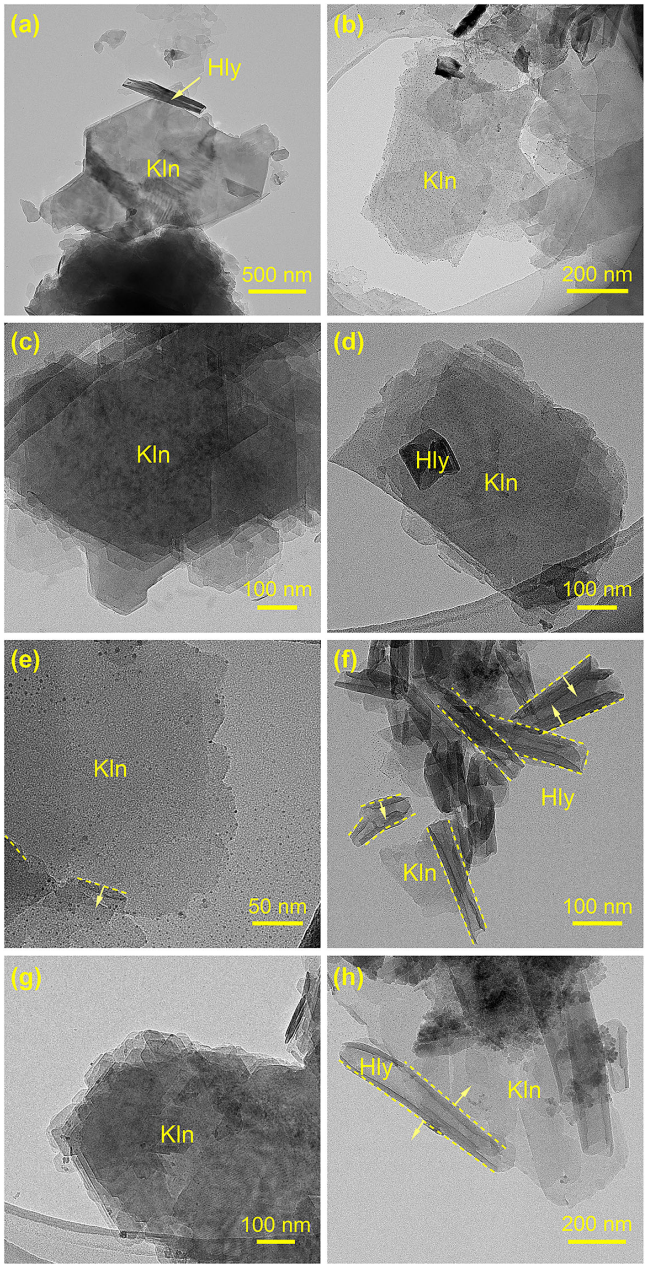

Figure 6. Transmission electron microscopy (TEM) images of kaolinite in (a–b) Section I, (c–d) Section II, (e–f) Section III-1, and (g–h) Section III-2. The dashed lines indicate rolled kaolinite, and the short arrows indicate the roll and unroll directions. Kln = kaolinite; Hly = halloysite.

Discussion

Effects of chemical weathering on the evolution of phyllosilicate minerals in regolith

The transformation process of phyllosilicate minerals in regolith layers is essentially related to chemical weathering intensity (Huang *et al.*, 2022), which can be described using the chemical index of alteration (CIA = $Al_2O_3/(Al_2O_3 + CaO + Na_2O + K_2O) \times 100$) (Nesbitt and Young, 1982). The CIA values of the Renju profile gradually increased at shallower depths (Fig. 1). Chemical weathering leads to the dissolution of primary minerals and the formation of secondary phyllosilicate minerals owing to the gradual loss of mobile elements, such as K, Na, Ca, and Si, and the accumulation of immobile elements such as Al (Banfield and Eggleton, 1990; Wilson, 2004). Consequently, the abundance of secondary phyllosilicate minerals increased with the progressive weathering of primary minerals in the regolith (Fig. 3).

Section I (CIA = 72–80) corresponded to the initial weathering stage. At this stage, secondary phyllosilicate minerals are formed in the following order, from primary minerals to 2:1 phyllosilicate minerals and then to 1:1 phyllosilicate minerals, or from primary minerals to 1:1 phyllosilicate minerals (Eggleton and Buseck, 1980; Senkayi *et al.*, 1984; Banfield and Eggleton, 1990), depending on the order and rate of elements released from primary rock-forming minerals (Chou and Wollast, 1984; Chou and Wollast, 1985; Muir *et al.*, 1990). Micas and plagioclase from bedrock were readily weathered into secondary phyllosilicate minerals in Section I, due to their relatively weak resistance to weathering (Banfield and Eggleton, 1990; Schroeder *et al.*, 2022). Orthoclase was the major rock-forming mineral in Section I that contributed to the increase of secondary phyllosilicates from Section I to III (Fig. 2 & Fig. 4a). Previous studies have shown that Al–O bonds demonstrate lower dissolution activation energy than Si–O bonds in plagioclase tetrahedra; therefore, Al tends to be released from plagioclase, to form a Si-rich layer at the plagioclase surface (Chou and Wollast, 1984; Casey *et al.*, 1989). The present study showed that the high Si/Al ratio of the Si-rich layer facilitated the formation of 2:1 phyllosilicate mineral (*e.g.* illite) when it reacted with the released Al cations in the ambient solution (Fig. 4a). The relatively low Si/Al ratio in the ambient solution possibly led to the formation of 1:1 phyllosilicate minerals (*e.g.* kaolinite and halloysite) (Chou and Wollast, 1984; Banfield and Eggleton, 1990; Devidal *et al.*, 1996). As a result, both the 2:1 and 1:1 phyllosilicate minerals formed due to the chemical weathering of orthoclase, as demonstrated by the positive correlation between the abundances of illite (2:1 type) and halloysite/kaolinite (1:1 type) in Section I (Fig. 7a; $R^2 = 0.85$).

Section II (CIA = 73–84) corresponded to the intermediate weathering stage. At this stage, the abundance of 2:1 illite significantly decreased in more weathered depths, whereas the total abundance of 1:1 halloysite and kaolinite gradually increased (Fig. 3), resulting in a negative correlation between the illite abundance and the total halloysite and kaolinite abundance (Fig. 7a; $R^2 = 0.96$). Accordingly, the 2:1 illite gradually transformed to 1:1 kaolinite and halloysite in the intermediate weathering stage (Fig. 4b), and the transformation could proceed via the mechanisms of dissolution-precipitation or solid-state transformation (Cuadros, 2012).

Effects of hydrological conditions on the mutual transformation between kaolinite and halloysite

Section III (CIA = 83–99) was mainly composed of kaolinite and halloysite with a small amount of illite, corresponding to the advanced weathering stage (Fig. 2). The weak correlation between the abundance of illite and the abundance of kaolinite and halloysite (Fig. 7a) was indicative of insignificant transformation of 2:1 phyllosilicate minerals to 1:1 phyllosilicate minerals at this weathering stage. Moreover, the abundance of kaolinite gradually decreased upward along the profile in Section III-1, but gradually increased in Section III-2 (Fig. 3). The negative correlation between the abundances of kaolinite and halloysite (Fig. 7b) suggested that kaolinite and halloysite underwent mutual transformation in Section III. As

https://doi.org/10.1017/cmn.2024.1 Published online by Cambridge University Press

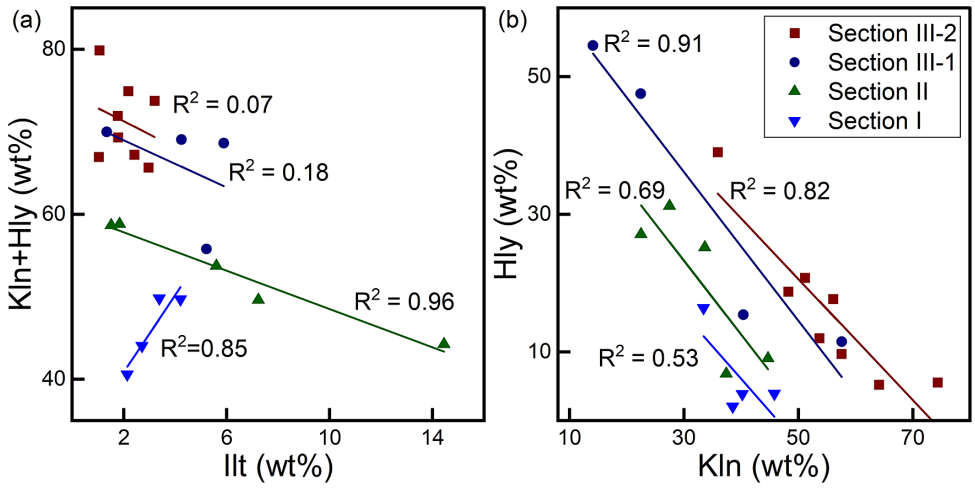

Figure 7. Plots of (a) kaolinite and halloysite abundance versus illite abundance, and (b) halloysite abundance versus kaolinite abundance in regolith samples.

halloysite usually forms in a wet environment while kaolinite favors a largely dry environment (Churchman *et al.*, 2016), the mutual transformation between kaolinite and halloysite can be attributed to variations in hydrological conditions.

Section III-1 was located in the vicinity of the vadose–saturated zone boundary (Fig. 1), where seasonal precipitation created an alternating wetting and drying zone (Pepper and Gentry, 2015). Kaolinite ($Al_2Si_2O_5(OH)_4$) is composed of one Si–O tetrahedral sheet and one Al–O octahedral sheet. Wetting can cause hydration of kaolinite by introducing interlayer water molecules (Churchman and Carr, 1975; Costanzo and Giese, 1985), thus disrupting the interlayer hydrogen bond and increasing the size of the Si–O tetrahedral sheet. The increased size of the Si–O tetrahedral sheet relative to the Al–O octahedral sheet possibly caused a mismatch between the apical oxygen plane and the inner OH plane (Radoslovich, 1963; Singh and Gilkes, 1992a; Singh, 1996; Bobos *et al.*, 2001), leading to bending and rolling of the 1:1 layers (Fig. 6e–f). The rolling axis was suggested to be parallel to the *b*-axis with the Al–O octahedral sheet as the inner surface (Singh and Mackinnon, 1996). In addition, drying could have induced the loss of lumen water (Santagata and Johnston, 2022), thereby creating evacuated lumen space for the inward rolling of the hydrated 1:1 layers (Fig. 6e–f). Therefore, the alternate wetting and drying condition facilitated the kaolinite-to-halloysite (K-to-H) transformation, which is consistent with the abrupt increase in halloysite abundance in Section III-1 (Fig. 3).

Section III-2 was located in the vadose zone (Fig. 1), where the soil moisture significantly decreased owing to infiltration and evaporation of vadose zone water (Wang *et al.*, 2017). The 1:1 layer of halloysite ($Al_2Si_2O_5(OH)_4 \cdot nH_2O$) features 0–2 interlayer H_2O molecules per unit cell. In the vadose zone, dehydration can cause the loss of interlayer H_2O molecules in halloysite under the sustained drying conditions (Kohyama *et al.*, 1978; Costanzo and Giese, 1985; Inoue *et al.*, 2012). With the loss of H_2O molecules, the interlayer hydrogen bond linking the OH groups on the octahedral basal surface and the tetrahedral oxygen could drive the rotation of the tetrahedron and resolve the volume mismatch between the tetrahedral and octahedral sheets (Radoslovich, 1963; Singh, 1996), thus facilitating the unrolling of tubular halloysite into lamellar kaolinite in Section III-2 (Fig. 6g,h). Therefore, the transformation of halloysite to kaolinite and the increase in kaolinite abundance in Section III-2 were probably induced by the dry environment of the vadose zone (Fig. 3).

Factors controlling variations in the structural order of kaolinite

Kaolinite structural disorder can be caused by layer displacement and octahedral vacancy displacement (Plançon *et al.*, 1989). In the Renju regolith, the HI values (0.27–0.78) were indicative of a range of high to medium defect levels for the kaolinite, while R2 values (0.79–1.05) suggest medium defect levels (Fig. 8) (Aparicio *et al.*, 2006). The $(1\bar{3}1)$ and (131) diffraction used for calculating R2 values are related to the variation of octahedral vacancy (Plançon and Zacharie, 1990). The variations of R2 values in kaolinite from different sections (Fig. 5) indicated variation in proportion of the octahedral vacancy order of kaolinite along the Renju profile. Besides, the HI values can be significantly reduced due to the presence of halloysite, particularly when halloysite is abundant (Aparicio and Galan, 1999); thus the discrepancy between the HI and R2 can be ascribed to the interference from halloysite throughout the Renju regolith (Fig. 8). Accordingly, R2 is more suitable for evaluating the structural order of kaolinite in Renju weathering regolith, as it could be less influenced by halloysite.

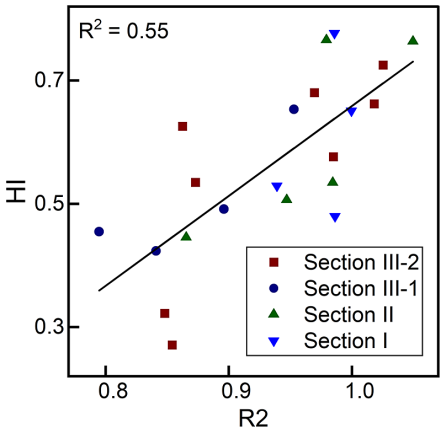

Figure 8. Plot of the Hinckley index (HI) versus the Liétard index (R2) in regolith samples.

https://doi.org/10.1017/cmn.2024.1 Published online by Cambridge University Press

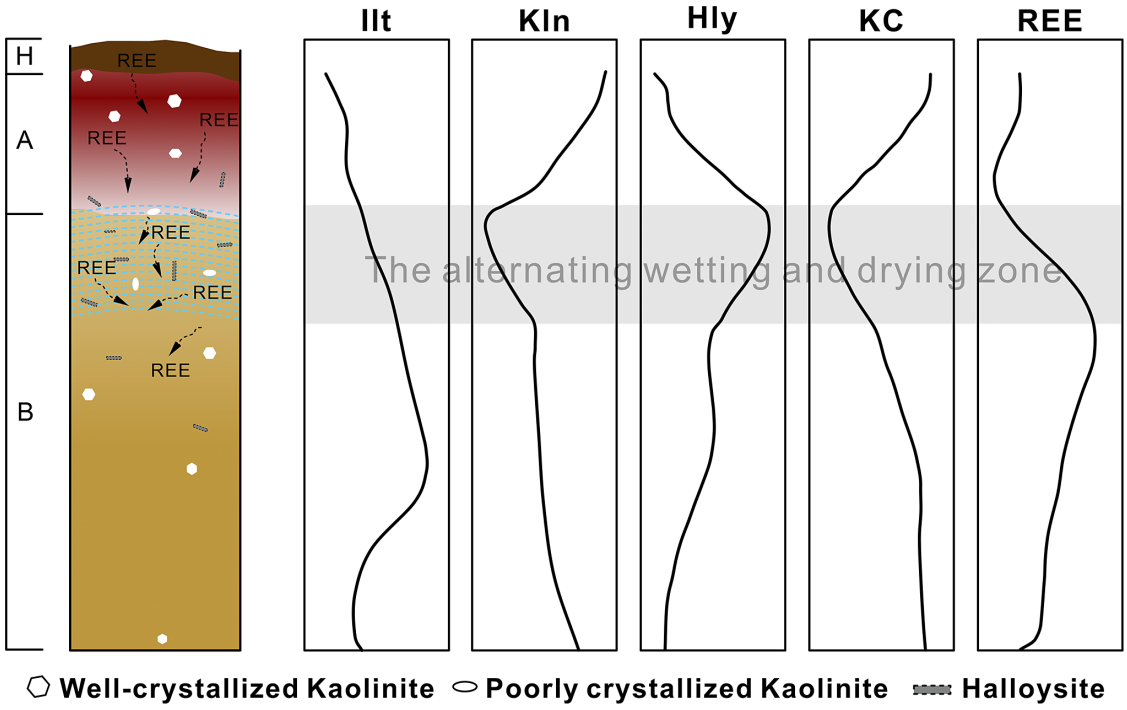

Figure 9. Schematic model illustrating the effects of the hydrodynamic conditions on the abundance of phyllosilicate minerals, kaolinite structural order, and REE enrichment. The shaded area represents the alternating wetting and drying zone. Kln = kaolinite abundance; Hly = halloysite abundance; Ilt = illite abundance; KC = kaolinite structural order; REE = REE concentration.

The kaolinite in Sections I and II was mainly composed of newly crystallized grains resulting from the dissolution of orthoclase and illite. The relatively stable physicochemical and hydrological conditions of Sections I and II provided a stable moisture and ionic strength environment (Huang *et al.*, 2021a) for kaolinite crystallization, thereby facilitating the formation of euhedral kaolinite grains (Fig. 6a–d). Consequently, kaolinite exhibited a stable structural order, and its abundance gradually increased at shallower depths in Sections I and II (Fig. 5).

In Section III-1, kaolinite exhibited an abrupt decrease in structural order compared with Section II. The kaolinites could possibly become more defective with time due to radioactive decay of surrounding K and Th (Mathian *et al.*, 2020), as kaolinite in Section III-1 was more aged than that in Section II. However, kaolinite from shallower Section III-2 was less defective than less weathered Section III-1, suggestive of the remarkable influence of hydrological conditions on the structural order of kaolinite in Section III. The decreased R2 values (Fig. 5c) indicated an increase in the disordered octahedral vacancies. During the K-to-H transformation, kaolinite reduced the distance between apical oxygens and the Si–O–Si angle in the tetrahedral sheet (Singh and Gilkes, 1992a; Singh, 1996) at the curly edges (Fig. 6f), and halloysite tubes were formed in the interstices of kaolinite (Fig. 4c). Kaolinite dissolution, as evidenced by the morphological features of round and irregular edges (Fig. 6e), probably facilitated the detachment and replacement of octahedral and tetrahedral cations (Wieland and Stumm, 1992; González Jesús *et al.*, 2000; Tyagi *et al.*, 2006), and tended to produce disordered octahedral vacancies (Sakharov *et al.*, 2016), thereby reducing kaolinite structural order. Consequently, the K-to-H transformation induced kaolinite dissolution in Section III-1 and reduced both the structural order and abundance of kaolinite.

In Section III-2, the dehydration of halloysite (Fig. 6h) strengthened the hydrogen bond between the dehydrated layers of halloysite and drove the rotation of the Si–O tetrahedra of halloysite about their apices in opposite directions, causing Si and O to move closer to the ditrigonal ring center (Singh, 1996). The unrolling of halloysite along the crystalline axis possibly led to an increase in the regularity of vacancy stacking (Plançon *et al.*, 1989; Fashina and Deng, 2021), as is displayed by the R2 values (Fig. 5c). Therefore, the decrease in the kaolinite defect density in Section III-2 was affected by the halloysite-to-kaolinite (H-to-K) transformation, and the stacking of well-crystallized triclinic kaolinite along the *c*-axis led to the formation of vermicular kaolinite in Section III-2 (Fig. 4d).

Underlying relationships between phyllosilicate mineral evolution and regolith-hosted REE mineralization

The vertical zonation of regolith can be defined by boundaries where the mineral composition and structural order of kaolinite became significantly varied. Previous studies suggested that changes in pH throughout the regolith largely influenced the adsorption capacity of phyllosilicate minerals and the distribution of REE mineralization (Bao and Zhao, 2008). However, the pH values change only between 4.7 and 6.3, and thus are unlikely to lead to significant changes in the adsorption capacity of phyllosilicate minerals of different sections in the studied regolith (Huang *et al.*, 2021a). A previous study reported REE enrichment at the transition zone between upper and lower pedolith, spatially coincident with mineral transformation between halloysite and kaolinite (Li and Zhou, 2020, 2023). In Renju regolith, REE enrichment started at the interface between Section III-1 and Section III-2, where the type of mineral transformation changed from K-to-H to H-to-K. Li and Zhou (2020) suggested that mineral transformation led to REE desorption in regolith-hosted REE deposit due to a decrease in

https://doi.org/10.1017/cmn.2024.1 Published online by Cambridge University Press

adsorption capacity, given the fact that poorly crystallized kaolinite in Section III-1 can provide more adsorption sites for REEs and facilitate the formation of REE ore body (Fialips *et al.*, 2000; Ndlovu *et al.*, 2015). However, the present study shows that the regolith above Section III-1 does not reach saturation regarding the adsorption of REEs (Table 1; Fig. 3), when evaluated with relatively underestimated adsorption capacity of kaolinite and other phyllosilicate minerals (Singh and Gilkes, 1992b). Therefore, the desorption of REE from Section III-2 and their enrichment in Section III-1 were probably influenced by other factors.

Note that the interface between Section III-1 and Section III-2 was characterized by mineral transformation and significant kaolinite structural order variation. The present study demonstrated that both the K-to-H transformation and kaolinite structural order were essentially related to the alternating wetting and drying hydrological condition (Keller, 1978; Hurst and Kunkle, 1985; Metz and Ganor, 2001). The fluctuations in water table were largely controlled by precipitation (Wang and Pozdniakov, 2014; Hussain *et al.*, 2022), thus creating the alternating wetting and drying hydrological condition between the highest and the lowest water table level within the regolith. As a result, REEs above the alternating wetting and drying interface were vertically transported by vadose zone water and fixed by phyllosilicate minerals around the water table owing to a significant decrease in the seepage velocity (Huang *et al.*, 2021a), resulting in poor REE content in Section III-2 and initial REE enrichment at the interface (Fig. 1). The fixed REE ions can be partially desorbed and transported downward owing to the decrease in the water level. Additionally, REE-oxyhydroxide nanoparticles could also migrate via intense downward leaching and accumulate near the water table (Calabrese *et al.*, 2018). Consequently, the REEs became significantly enriched in the lowest level of the water table (Fig. 1 & Fig. 9). Therefore, hydrodynamic conditions controlled both the REE enrichment and the kaolinite structural order in the Renju profile, forming the spatial coupling among the alternating wetting and drying zone, REE enrichment and mineral structural order (Fig. 9). Accordingly, the kaolinite structural order indices can be utilized to indicate the location of the regolith-hosted REE deposit in the weathering regolith (Fig. 9).

Conclusions

This study investigated the variations in the abundance of phyllosilicate minerals and the structural order of kaolinite in the regolith. The weathering of the primary mineral orthoclase and 2:1 phyllosilicate mineral was influenced by the intensity of chemical weathering. The hydrological conditions in the Renju regolith can explain well the abrupt changes in both the abundance and structural order of kaolinite in Section III. In the region around the vadose–saturated zone boundary, an alternating wetting and drying zone provided a favorable kinetic environment for intensive kaolinite-to-halloysite transformation and kaolinite dissolution. The decrease in abundance of kaolinite in Section III-1 coincided with the decrease in structural order of kaolinite during kaolinite-to-halloysite transformation and kaolinite dissolution. As soil moisture decreased in the vadose zone, halloysite lost its interlayer water and underwent dehydration to form well-crystallized kaolinite. Accordingly, this work would be the first documented case of the occurrence of mutual transformation between kaolinite and halloysite at Earth's surface conditions. The REEs were transported vertically by vadose water to the highest water table level, then moved along with the fluctuating water tables and formed prominent REE enrichment at the lowest water table level in Section III-1. Hydrodynamic conditions affected both kaolinite transformation and REE enrichment; a low kaolinite abundance and structural order can serve as an indicator of alternating wetting and drying zones and the occurrence of regolith-hosted REE mineralization in a weathering regolith.

Supplementary material. The supplementary material for this article can be found at https://doi.org/10.1017/cmn.2024.1.

Acknowledgements. Constructive comments by the Editor-in-Chief, Dr Joseph W. Stucki, the Associate Editor, and three anonymous reviewers, helped improve the manuscript. This is contribution No.IS-3501 from Guangzhou Institute of Geochemistry, Chinese Academy of Sciences.

Financial support. This work was supported by the National Natural Science Foundation of China (grant No. 41921003 and 42022012), the National Key R&D Program of China (grant No. 2021YFC2901701) the Youth Innovation Promotion Association CAS (grant No. 2023369), Science and Technology Planning of Guangdong Province, China (grant No. 2023B1212060048), and the Technology & Geology Planning Project of Jiangxi Province, China (grant No. 2023KDG01006).

Competing interest. The authors declare that they have no competing interests.

References

Aparicio, P., & Galan, E. (1999). Mineralogical interference on kaolinite crystallinity index measurements. *Clays and Clay Minerals*, *47*, 12–27.

Aparicio, P., Galán, E., & Ferrell, R.E. (2006). A new kaolinite order index based on XRD profile fitting. *Clay Minerals*, *41*, 811–817.

Banfield, J.F., & Eggleton, R.A. (1990). Analytical transmission electron microscope studies of plagioclase, muscovite, and K-feldspar weathering. *Clays and Clay Minerals*, *38*, 77–89.

Bao, Z.W., & Zhao, Z.H. (2008). Geochemistry of mineralization with exchangeable REY in the weathering crusts of granitic rocks in south China. *Ore Geology Reviews*, *33*, 519–535.

Bauluz, B., Mayayo, M.J., Yuste, A., & Gonzalez Lopez, J.M. (2008). Genesis of kaolinite from Albian sedimentary deposits of the Iberian Range (NE Spain): analysis by XRD, SEM and TEM. *Clay Minerals*, *43*, 459–475.

Blanton, T., & Gates-Rector, S. (2019). The Powder Diffraction File: a quality materials characterization database. *Powder Diffraction*, *34*, 352–360.

Bobos, I., Duplay, J., Rocha, J., & Gomes, C. (2001). Kaolinite to halloysite-7 Å transformation in the kaolin deposit of São Vicente de Pereira, *Portugal.* Clays and Clay Minerals, *49*, 596–607.

Borst, A.M., Smith, M.P., Finch, A.A., Estrade, G., Villanova-de-Benavent, C., Nason, P., Marquis, E., Horsburgh, N.J., Goodenough, K.M., Xu, C., Kynicky, J., & Geraki, K. (2020). Adsorption of rare earth elements in regolith-hosted clay deposits. *Nature Communications*, *11*, 4386.

Calabrese, S., Richter, D.D. & Porporato, A. (2018). The formation of clay-enriched horizons by lessivage. *Geophysical Research Letters*, *45*, 7588–7595.

Casey, W.H., Westrich, H.R., Arnold, G.W., & Banfield, J.F. (1989). The surface chemistry of dissolving labradorite feldspar. *Geochimica et Cosmochimica Acta*, *53*, 821–832.

Chou, L., & Wollast, R. (1984). Study of the weathering of albite at room temperature and pressure with a fluidized bed reactor. *Geochimica et Cosmochimica Acta*, *48*, 2205–2217.

Chou, L., & Wollast, R. (1985). Steady-state kinetics and dissolution mechanisms of albite. *American Journal of Science*, *285*, 963–993.

Chung, F.H. (1974). Quantitative interpretation of X-ray diffraction patterns of mixtures. I. Matrix-flushing method for quantitative multicomponent analysis. *Journal of Applied Crystallography*, *7*, 519–525.

Churchman, G.J., & Carr, R.M. (1975). The definition and nomenclature of halloysites. *Clays and Clay Minerals*, *23*, 382–388.

Churchman, G.J., & Gilkes, R.J. (1989). Recognition of intermediates in the possible transformation of halloysite to kaolinite in weathering profiles. *Clay Minerals*, *24*, 579–590.

Churchman, G.J., Pasbakhsh, P., Lowe, D.J., & Theng, B.K.G. (2016). Unique but diverse: some observations on the formation, structure and morphology of halloysite. *Clay Minerals*, *51*, 395–416.

Churchman, G.J., & Theng, B.K.G. (1984). Interactions of halloysites with amides; mineralogical factors affecting complex formation. *Clay Minerals*, *19*, 161–175.

Churchman, G.J., Whitton, J.S., Claridge, G.G.C., & Theng, B.K.G. (1984). Intercalation method using formamide for differentiating halloysite form kaolinite. *Clays and Clay Minerals*, *32*, 241–248.

Costanzo, P.M., & Giese, R.F. (1985). Dehydration of synthetic hydrated kaolinites: a model for the dehydration of halloysite (10 Å). *Clays and Clay Minerals*, *33*, 415–423.

Cuadros, J. (2012). Clay crystal-chemical adaptability and transformation mechanisms. *Clay Minerals*, *47*, 147–164.

Devidal, J.-L., Dandurand, J.-L., & Gout, R. (1996). Gibbs free energy of formation of kaolinite from solubility measurement in basic solution between 60 and 170°C. *Geochimica et Cosmochimica Acta*, *60*, 553–564.

Eggleton, R.A. & Buseck, P.R. (1980). High resolution electron microscopy of feldspar weathering. *Clays and Clay Minerals*, *28*, 173–178.

Fashina, B., & Deng, Y. (2021). Stacking disorder and reactivity of kaolinites. *Clays and Clay Minerals*, *69*, 354–365.

Fialips, C.-I., Petit, S., Decarreau, A., & Beaufort, D. (2000). Influence of synthesis pH on kaolinite 'crystallinity' and surface properties. *Clays and Clay Minerals*, *48*, 173–184.

González Jesús, J., Huertas, F.J., Linares, J., & Ruiz Cruz, M.D. (2000). Textural and structural transformations of kaolinites in aqueous solutions at 200°C. *Applied Clay Science*, *17*, 245–263.

He, H.P., Yuan, P., Guo, J.G., Zhu, J.X., & Hu, C. (2005). The influence of random defect density on the thermal stability of kaolinites. *Journal of the American Ceramic Society*, *88*, 1017–1019.

Hinckley, D.N. (1962). Variability in 'crystallinity' values among the kaolin deposits of the coastal plain of Georgia and South Carolina. *Clays and Clay Minerals*, *11*, 229–235.

Huang, J., He, H.P., Tan, W., Liang, X.L., Ma, L.Y., Wang, Y.Y., Qin, X.R., & Zhu, J.X. (2021a). Groundwater controls REE mineralisation in the regolith of South China. *Chemical Geology*, *577*, 120295.

Huang, J., Tan, W., Liang, X. L., He, H.P., Ma, L.Y., Bao, Z.W., & Zhu, J.X. (2021b). REE fractionation controlled by REE speciation during formation of the Renju regolith-hosted REE deposits in Guangdong Province, South China. *Ore Geology Reviews*, *134*, 104172.

Huang, J., Tan, W., Liang, X.L., He, H.P., Ma, L.Y., Bao, Z.W., Zhu, J.X., & Zhou, Q. (2022). Weathering characters of REE-bearing accessory minerals and their effects on REE mineralization in Renju regolith-hosted REE deposits in Guangdong Province (in Chinese). *Geochimica*, *51*, 684–695.

Hurst, V.J., & Kunkle, A.C. (1985). Dehydroxylation, rehydroxylation, and stability of kaolinite. *Clays and Clay Minerals*, *33*, 1–14.

Hussain, F., Wu, R.-S., & Shih, D.-S. (2022). Water table response to rainfall and groundwater simulation using physics-based numerical model: WASH123D. *Journal of Hydrology: Regional Studies*, *39*, 100988.

Inoue, A., Utada, M., & Hatta, T. (2012). Halloysite-to-kaolinite transformation by dissolution and recrystallization during weathering of crystalline rocks. *Clay Minerals*, *47*, 373–390.

Ishida, D.A., Vieira-Coelho, A.C., Melfi, A.J., Lucas, Y., Camargo, J.P.B., & Montes, C.R. (2018). Influence of pedogenetic processes on the validity of kaolinite crystallinity indices: a case study of an Amazonian Ferralsol-Podzol soil system with white kaolin. *Applied Clay Science*, *162*, 435–442.

Joussein, E., Petit, S., Fialips, C.-I., Vieillard, P. & Righi, D. (2006). Differences in the dehydration-rehydration behavior of halloysites: new evidence and interpretations. *Clays and Clay Minerals*, *54*, 473–484.

Jowitt, S.M., Wong, V.N.L., Wilson, S.A., & Gore, O. (2017). Critical metals in the critical zone: controls, resources and future prospectivity of regolith-hosted rare earth elements. *Australian Journal of Earth Sciences*, *64*, 1045–1054.

Keller, W.D. (1978). Kaolinization of feldspar as displayed in scanning electron micrographs. *Geology*, *6*, 184–188.

Kohyama, N., Fukushima, K., & Fukami, A. (1978). Observation of the hydrated form of tubular halloysite by an electron microscope equipped with an environmental cell. *Clays and Clay Minerals*, *26*, 25–40.

Li, M.Y.H., & Zhou, M.-F. (2020). The role of clay minerals in formation of the regolith-hosted heavy rare earth element deposits. *American Mineralogist*, *105*, 92–108.

Li, M.Y.H., & Zhou, M.-F. (2023). Physicochemical variation of clay minerals and enrichment of rare earth elements in regolith-hosted deposits: exemplification from the Bankeng deposit in south China. *Clays and Clay Minerals*, *71*, 362–376.

Li, Y.H.M., Zhao, W.W., & Zhou, M.-F. (2017). Nature of parent rocks, mineralization styles and ore genesis of regolith-hosted REE deposits in South China: an integrated genetic model. *Journal of Asian Earth Sciences*, *148*, 65–95.

Liétard, O. (1977). *Contribution à l'étude des proprités physicochimiques cristallographiques et morphologiques des kaolins*. PhD thesis, Université Institut National Polytechnique de Lorraine, Nancy, France, 345 pp.

Mathian, M., Bueno, G.T., Balan, E., Fritsch, E., Do Nascimento, N.R., Selo, M., & Allard, T. (2020). Kaolinite dating from Acrisol and Ferralsol: a new key to understanding the landscape evolution in NW Amazonia (Brazil). *Geoderma*, *370*, 114354.

McQueen, K. & Scott, K.M. (2008). Chapter 6: Rock weathering and structure of the regolith. In K.M. Scott, and C.F. Pain (eds), *Regolith Science* (1st edn) (pp. 103–124). CSIRO Publishing, Australia.

Mei, H., Jian, X., Zhang, W., Fu, H., & Zhang, S. (2021). Behavioral differences between weathering and pedogenesis in a subtropical humid granitic terrain: Implications for chemical weathering intensity evaluation. *CATENA*, *203*, 105368.

Metz, V., & Ganor, J. (2001). Stirring effect on kaolinite dissolution rate. *Geochimica et Cosmochimica Acta*, *65*, 3475–3490.

Muir, I.J., Bancroft, G.M., Shotyk, W., & Nesbitt, H.W. (1990). A SIMS and XPS study of dissolving plagioclase. *Geochimica et Cosmochimica Acta*, *54*, 2247–2256.

Ndlovu, B., Farrokhpay, S., Forbes, E., & Bradshaw, D. (2015). Characterisation of kaolinite colloidal and flow behaviour via crystallinity measurements. *Powder Technology*, *269*, 505–512.

Nesbitt, H.W., & Young, G.M. (1982). Early Proterozoic climates and plate motions inferred from major element chemistry of lutites. *Nature*, *299*, 715–717.

Ni, X., Zhao, Z., Li, Z., & Li, Q. (2021). The adsorptive behaviour of kaolinite to sodium dodecyl benzene sulphonate and the structural variation of kaolinite. *Scientific Reports*, *11*, 1796.

Pepper, I.L., & Gentry, T.J. (2015). Chapter 4: Earth environments. In I.L. Pepper, C.P. Gerba, & T.J. Gentry (eds), *Environmental Microbiology* (3rd edn) (pp. 59–88). Academic Press, San Diego.

Pineau, M., Mathian, M., Baron, F., Rondeau, B., Le Deit, L., Allard, T., & Mangold, N. (2022). Estimating kaolinite crystallinity using near-infrared spectroscopy: Implications for its geology on Earth and Mars. *American Mineralogist*, *107*, 1453–1469.

Plançon, A., Giese, R.F., Snyder, R., Drits, V.A., & Bookin, A.S. (1989). Stacking faults in the kaolin-group minerals: defect structures of kaolinite. *Clays and Clay Minerals*, *37*, 203–210.

Plançon, A., & Zacharie, C. (1990). An expert system for the structural characterization of kaolinites. *Clay Minerals*, *25*, 249–260.

Radoslovich, E.W. (1963). The cell dimensions and symmetry of layer-lattice silicates. VI. Serpentine and kaolin morphology. *American Mineralogist*, *48*, 368–378.

Regional Geological Survey Team of Jiangxi Geological Bureau (1976). Report of 1:200,000 regional geological survey of the Xunwu region: Anyuan [in Chinese].

Riesgo García, M.V., Krzemień, A., Manzanedo del Campo, M.Á., Menéndez Álvarez, M., & Gent, M.R. (2017). Rare earth elements mining investment: it is not all about China. *Resources Policy*, *53*, 66–76.

Sakharov, B.A., Drits, V.A., McCarty, D.K., & Walker, G.M. (2016). Modeling powder X-ray diffraction patterns of the clay minerals society kaolinite standards: KGa-1, KGa-1b, and KGa-2. *Clays and Clay Minerals*, *64*, 314–333.

Santagata, M., & Johnston, C.T. (2022). A study of nanoconfined water in halloysite. *Applied Clay Science*, *221*, 106467.

Schroeder, P.A. (2018). Chapter 1: What are clays and what is the critical zone? In P.A. Schroeder (ed), *Clays in the Critical Zone* (pp. 1–30). Cambridge University Press, Cambridge.

https://doi.org/10.1017/cmn.2024.1 Published online by Cambridge University Press

Schroeder, P.A., Austin, J.C., Thompson, A. & Richter, D.D. (2022). Mineralogical and elemental trends in regolith on historically managed sites in the southeastern United States piedmont. *Clays and Clay Minerals*, *70*, 539–554.

Senkayi, A.L., Dixon, J.B., Hossner, L.R., Abder-Ruhman, M., & Fanning, D.S. (1984). Mineralogy and genetic relationships of tonstein, bentonite, and lignitic strata in the Eocene Yegua Formation of east-central Texas. *Clays and Clay Minerals*, *32*, 259–271.

Simandl, G.J. (2014). Geology and market-dependent significance of rare earth element resources. *Mineralium Deposita*, *49*, 889–904.

Singh, B. (1996). Why does halloysite roll? – a new model. *Clays and Clay Minerals*, *44*, 191–196.

Singh, B., & Gilkes, R.J. (1992a). An electron optical investigation of the alteration of kaolinite to halloysite. *Clays and Clay Minerals*, *40*, 212–229.

Singh, B., & Gilkes, R.J. (1992b). Properties of soil kaolinites from south-western Australia. *Journal of Soil Science*, *43*, 645–667.

Singh, B., & Mackinnon, I.D.R. (1996). Experimental transformation of kaolinite to halloysite. *Clays and Clay Minerals*, *44*, 825–834.

Tan, W., Qin, X.R., Liu, J.C., Michalski, J., He, H.P., Yao, Y.Z., Yang, M.J., Huang, J., Lin, X.J., Zhang, C.Q., & Liang, X.L. (2021). Visible/near infrared reflectance (VNIR) spectral features of ion-exchangeable rare earth elements hosted by clay minerals: potential use for exploration of regolith-hosted REE deposits. *Applied Clay Science*, *215*, 106320.

Tyagi, B., Chudasama, C.D., & Jasra, R.V. (2006). Determination of structural modification in acid activated montmorillonite clay by FT-IR spectroscopy. *Spectrochimica Acta Part A: Molecular and Biomolecular Spectroscopy*, *64*, 273–278.

Wang, P., & Pozdniakov, S.P. (2014). A statistical approach to estimating evapotranspiration from diurnal groundwater level fluctuations. *Water Resources Research*, *50*, 2276–2292.

Wang, W., Zhang, Z., Yeh, T.-c.J., Qiao, G., Wang, W., Duan, L., Huang, S.-Y., & Wen, J.-C. (2017). Flow dynamics in vadose zones with and without vegetation in an arid region. *Advances in Water Resources*, *106*, 68–79.

Wang, Z., & Xu, J. (2016). Characteristics and prevention measures of soil erosion in Renju rare earth mining area in northern Guangdong province [in Chinese]. *Subtropical Soil and Water Conservation*, *28*, 51–56.

Weng, Z., Jowitt, S.M., Mudd, G.M., & Haque, N. (2015). A detailed assessment of global rare earth element resources: opportunities and challenges. *Economic Geology*, *110*, 1925–1952.

Wieland, E., & Stumm, W. (1992). Dissolution kinetics of kaolinite in acidic aqueous solutions at 25°C. *Geochimica et Cosmochimica Acta*, *56*, 3339–3355.

Wilson, J. (2004). Weathering of the primary rock-forming minerals: processes, products and rates. *Clay Minerals*, *39*, 233–266.

Wu, F., Fang, X., Yang, Y., Dupont-Nivet, G., Nie, J., Fluteau, F., Zhang, T., & Han, W. (2022). Reorganization of Asian climate in relation to Tibetan plateau uplift. *Nature Reviews Earth & Environment*, *3*, 684–700.

Xu, C., Kynicky, J., Smith, M.P., Kopriva, A., Brtnicky, M., Urubek, T., Yang, Y. H., Zhao, Z., He, C., & Song, W.L. (2017). Origin of heavy rare earth mineralization in South China. *Nature Communications*, *8*, 14598.

Yang, D., & Xiao, G. (2011). Regional metallogenic regularities of the ion adsorption type of rare-earth deposits in Guangdong province [in Chinese]. *Geology and Resources*, *20*, 462–468.

Yang, M.J., Liang, X.L., Ma, L.Y., Huang, J., He, H.P., & Zhu, J.X. (2019). Adsorption of REEs on kaolinite and halloysite: a link to the REE distribution on clays in the weathering crust of granite. *Chemical Geology*, *525*, 210–217.

Zadvernyuk, H., Kadoshnikov, V., Shekhunova, S., & Remez, S. (2021). Particle size distribution and crystallinity as indicators of kaolinite genesis. *Applied Clay Science*, *213*, 106236.

Zhao, X., Li, N.-B., Huizenga, J.M., Yan, S., Yang, Y.-Y., & Niu, H.-C. (2021). Rare earth element enrichment in the ion-adsorption deposits associated granites at Mesozoic extensional tectonic setting in South China. *Ore Geology Reviews*, *137*, 104317.

https://doi.org/10.1017/cmn.2024.1 Published online by Cambridge University Press